Spin-valley coupling and spin-relaxation anisotropy in all-CVD Graphene-MoS2 van der Waals heterostructure

Spin-valley coupling and spin-relaxation anisotropy in all-CVD Graphene-MoS_2 van der Waals heterostructure

Anamul Md. Hoque,[1] Vasudev Ramachandra,[1] Antony George,[2] Emad Najafidehaghani,[2] Ziyang Gan,[2] Richa Mitra,[1] Bing Zhao,[1] Dmitrii Khokhriakov,[1] Andrey Turchanin,[2] Samuel Lara-Avila,[1] Sergey Kubatkin,[1] and Saroj P. Dash[1,*]

[1]*Department of Microtechnology and Nanoscience, Chalmers University of Technology, SE-41296 Göteborg, Sweden*

[2]*Friedrich Schiller University Jena, Institute of Physical Chemistry, 07743 Jena, Germany*

(Received 3 September 2022; accepted 22 March 2023; published 24 April 2023)

Two-dimensional (2D) van der Waals (vdW) heterostructures fabricated by combining 2D materials with unique properties into one ultimate unit can offer a plethora of fundamental phenomena and practical applications. Recently, proximity-induced quantum and spintronic effects have been realized in heterostructures of graphene (Gr) with 2D semiconductors and their twisted systems. However, these studies are so far limited to exfoliated flake-based devices, limiting their potential for scalable practical applications. Here, we report spin-valley coupling and spin-relaxation anisotropy in Gr-MoS_2 heterostructure devices prepared from scalable chemical vapor-deposited (CVD) 2D materials. Spin precession and dynamics measurements reveal an enhanced spin-orbit coupling strength in the Gr-MoS_2 heterostructure in comparison with pristine Gr at room temperature. Consequently, large spin-relaxation anisotropy is observed in the heterostructure, providing a method for spin filtering due to spin-valley coupling. These findings open a scalable platform for all-CVD 2D vdW heterostructures design and their device applications.

DOI: 10.1103/PhysRevMaterials.7.044005

I. INTRODUCTION

Two-dimensional (2D) materials host unique charges, spins, and orbital degrees of freedom that can be uniquely manipulated in van der Waals (vdW) heterostructures for quantum and spintronic applications [1–7]. Graphene (Gr) is well known for hosting Dirac fermions and high carrier mobility along with long-distance spin transport due to its low spin-orbit coupling (SOC) property [8–13]. However, significant efforts have been made to enhance SOC in Gr to realize gate-tunable spintronic functionalities [14]. One way to achieve sizable SOC in Gr is by employing chemically adsorbed heavy adatoms [15,16]; nevertheless, doping can introduce defects in Gr and compromise the fascinating electronic properties [17]. Alternatively, the vdW heterostructures of Gr with high-SOC 2D materials, such as transition metal dichalcogenides (TMDCs) [18–21], Rashba materials [22], and topological insulators (TIs), have emerged as promising platforms for proximity-induced SOC [23,24] while preserving their electronic properties [25–29]. Moreover, introducing SOC in twisted Gr heterostructures can yield correlated electronic phases and quantum phenomena [30,31].

The signatures of the increased SOC demonstrate the potential of Gr-TMDC heterostructures in quantum and spintronic devices [24,32]. First, an increase of SOC strength in Gr-TMDCs, its gate modulation and hydrostatic pressure dependence are demonstrated at low temperatures [33–37]. The spin transport in Gr-MoS_2 heterostructures revealed spin field-effect modulation functionality up to room temperature, where the spin signal could be controlled by a gate electric field [38,39]. Moreover, valley-polarized spin injection and proximity-induced spin Hall and Rashba-Edelstein effects have been realized in Gr-TMDC heterostructures [40–44]. Another exciting aspect of proximity-induced SOC in Gr is the spin-lifetime anisotropy, which results in spin-filtering functionalities due to the different spin-relaxation times for spins in different orientations [45]. However, experimental reports on the spin-valley coupling are so far limited to exfoliated flakes, and realization in a scalable Gr-TMDC heterostructure is still missing and challenging as well due to the complex fabrication process.

Here, we report spin transport and dynamics in scalable Gr-MoS_2 vdW heterostructure spintronic devices grown by chemical vapor deposition (CVD) methods. The CVD-grown materials and their vdW heterostructure devices show excellent charge transport properties. Spin transport and precession properties were investigated in the heterostructure channel using a nonlocal (NL) spin valve (SV) and Hanle spin-precession measurements at room temperature. Detailed oblique field dependence of spin-precession measurements are performed to estimate spin-valley coupling and spin-relaxation anisotropy. These studies open a scalable platform for all-CVD 2D heterostructure-based devices.

*saroj.dash@chalmers.se

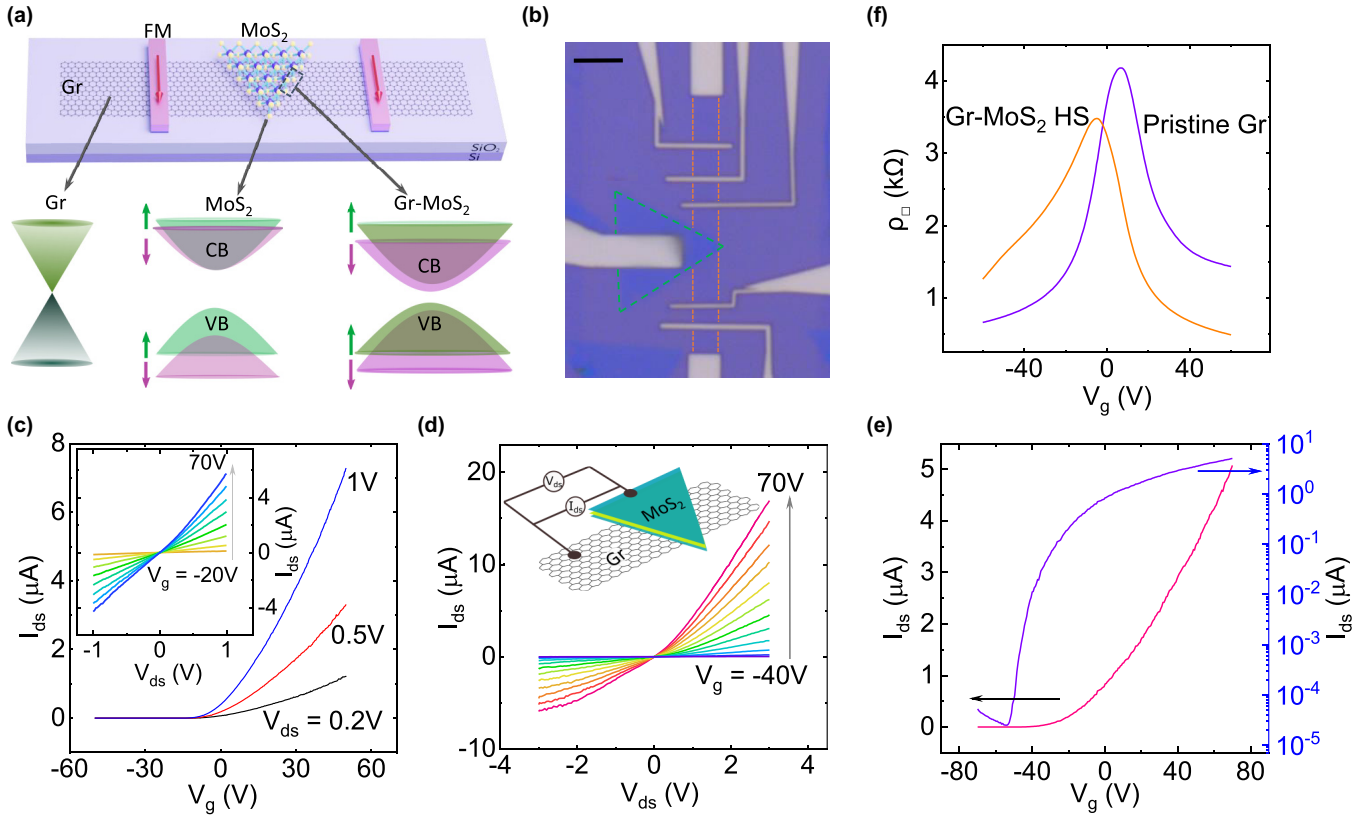

FIG. 1. All–chemical vapor-deposited (CVD) graphene (Gr)-MoS_2 heterostructure spintronic device and electrical properties. (a) Schematic representation of the Gr and MoS_2 van der Waals (vdW) heterostructure device on Si/SiO_2 substrate along with the ferromagnetic (FM) contacts. Pictorial depiction of the band diagram of Gr, MoS_2, and their heterostructure with spin-split bands. (b) Optical image of CVD-Gr (orange dotted line) and CVD-MoS_2 (green dotted line) vdW heterostructure along with the different FM contacts. The scale bar is 5 μm. The width and shapes of the FM contacts are designed on Gr to facilitate spin injection and detection. (c) Source-drain current I_{ds} as a function of the applied backgate voltage (V_g) of single layer of CVD-MoS_2 field-effect transistor with different source-drain bias voltages V_{ds}. Inset shows I_{ds} vs V_{ds} at different V_g. (d) I_{ds} vs V_{ds} plots at different gate voltages between Gr-MoS_2 along with the measurement geometry in the inset. (e) Transfer properties (I_{ds} vs V_g) between Gr-MoS_2 at $V_{ds} = 1$ V in linear (pink) and log (violet) scale. (f) Gate-dependent resistivity of Gr channels in pristine and heterostructure regions probed with four-terminal measurement geometry.

II. RESULTS AND DISCUSSION

A. All-CVD Gr-MoS_2 heterostructure device fabrication and electrical characterization

Figure 1(a) shows the schematic of a device structure consisting of a CVD-grown Gr-MoS_2 heterostructure on a Si/SiO_2 substrate, which allows us to apply backgate voltage (V_g). The bottom panel in Fig. 1(a) illustrates the band diagram of Gr and MoS_2 with spin-split bands for up and down spins [46,47]. MoS_2 in the Gr-MoS_2 vdW heterostructure region can induce spin-valley SOC in Gr via the proximity effect and modify the band structure and spin transport in the channel [26,48]. An optical micrograph of a fabricated device is presented in Fig. 1(b), where the monolayer CVD-Gr channel is covered with a monolayer CVD-MoS_2, which was transferred by a wet transfer technique [49]. Subsequently, e-beam lithography was performed to make ferromagnetic (FM) tunnel contacts of TiO_2 (∼1 nm)/Co (∼80 nm) suitable for studying charge and spin-transport properties in the devices (see the Methods for details).

First, we describe the characterization of the individual CVD-grown monolayer materials to inspect their electrical properties. The transport properties (source-drain current I_{ds} vs gate voltage V_g) of MoS_2 are depicted in Fig. 1(c) for different bias voltages V_{ds}, along with I_{ds} vs V_{ds} at different V_g in the inset. Here, I_{ds} increases monotonically with increasing V_{ds}, and I_{ds} increases with increasing V_g for fixed V_{ds} due to increasing carrier concentration in the MoS_2, which corresponds to *n*-type transport properties [50]. We estimated the field-effect mobility $\mu = \frac{Lg_m}{WC_gV_{ds}} = 1.21\,\mathrm{cm^2\,V^{-1}\,s^{-1}}$; where L, W, C_g, and g_m are the channel length, width, gate capacitance per area ($1.15 \times 10^{-8}\,\mathrm{F\,cm^{-2}}$ for 285-nm SiO_2), and transconductance, respectively.

Next, charge transport properties are measured for the Gr-MoS_2 vdW junction. Figure 1(d) shows the measured I_{ds} as a function of applied V_{ds} at various V_g along with the measurement geometry. The asymmetric I_{ds}-V_{ds} properties with diodelike behavior could be attributed to the work function mismatch between the electrodes and the materials [51,52]. The transfer characteristic (I_{ds} vs V_g) of the Gr-MoS_2 heterostructure for $V_{ds} = 1$ V is depicted in Fig. 1(e). We found an increase of I_{ds} with increasing positive V_g that is derived mainly from the transport properties of MoS_2, where Gr acts as a vdW contact. The field-effect mobility μ is estimated to

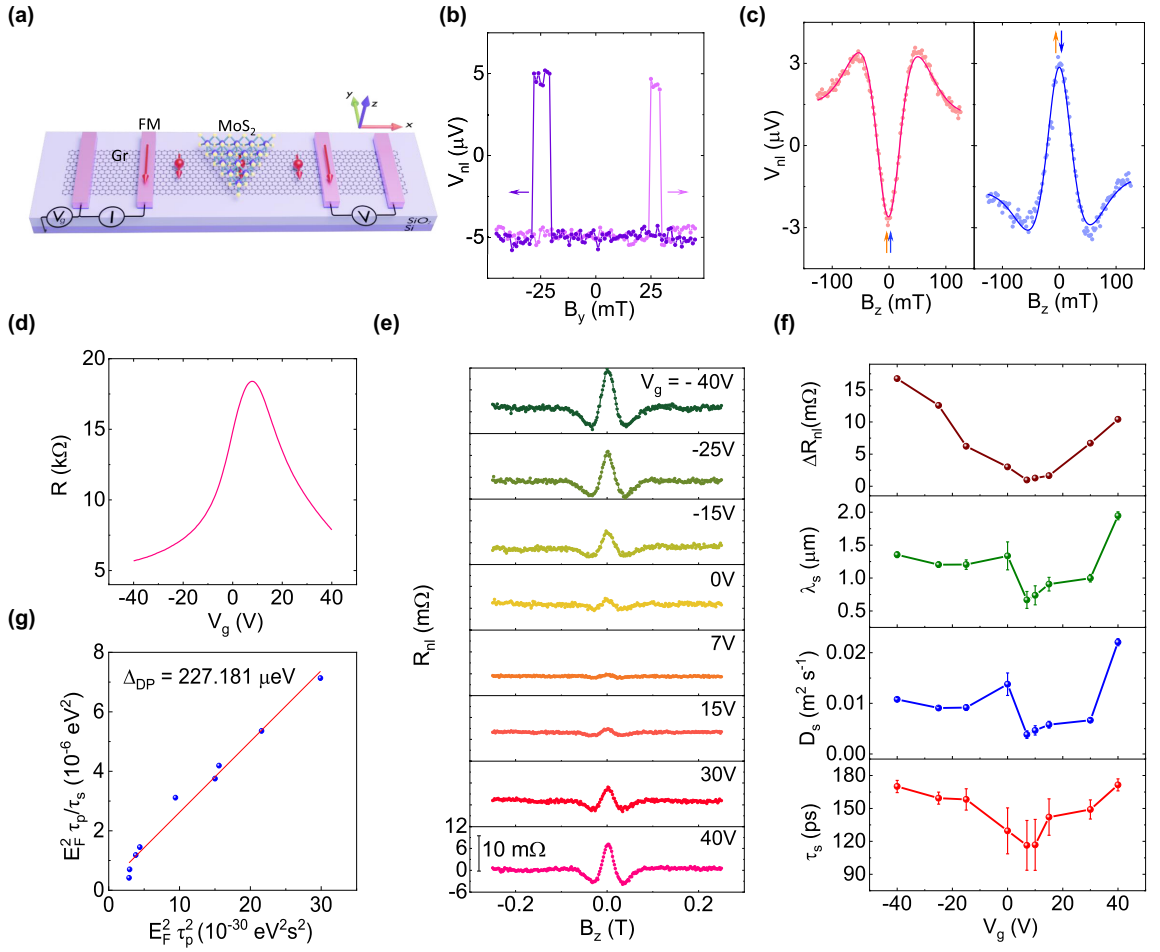

FIG. 2. Spin transport and precession across the all–chemical vapor-deposited (CVD) graphene-MoS_2 heterostructure at room temperature. (a) Schematic of the nonlocal (NL) measurement geometry to measure spin transport and precession in Gr-MoS_2 heterostructure region. (b) NL spin-valve (NLSV) signal with changing magnetic field along the y axis. Up and down magnetic field sweep directions are indicated by the arrows. (c) Hanle spin-precession signals with out-of-field magnetic field sweep and the data fittings (solid lines) to estimate spin parameters in the heterostructure region for parallel and antiparallel magnetization of the ferromagnetic (FM) electrodes. Measurements were performed in Device 1 with $I = -250\,\mu$A and $V_g = 60$ V, and a small linear background is subtracted from the data. (d) Gate-dependent Gr channel resistance in the Gr-MoS_2 heterostructure. The Dirac point of Gr in this Gr-MoS_2 heterostructure channel is 7 V. (e) Evolution of Hanle spin-precession signal in Gr-MoS_2 heterostructure measured at different V_g in Device 2 with $I = -400\,\mu$A. The scale bar for the magnitude of the signal R_{nl} is 10 mΩ. (f) Gate dependence of the Hanle spin-precession signal amplitude (ΔR_{nl}), spin-diffusion length (λ_s), diffusion constant (D_s), and spin lifetime (τ_s). (g) Estimation of spin-orbit coupling (SOC) strength in Gr-MoS_2 heterostructure along with fitting (solid line) to Eq. (2).

be 4.06 $cm^2\,V^{-1}\,s^{-1}$ in the Gr-MoS_2 heterostructure, which is ∼3× higher than in pristine MoS_2 with metallic contacts. This mobility enhancement of MoS_2 field-effect transistor with Gr contact can be attributed to reduced defect states in the MoS_2 contact region and lower Schottky barrier at the Gr-MoS_2 vdW interface [52–54]. Figure 1(f) presents the gate-dependent Gr resistivity ($\rho_\square = \frac{R_{4T}W}{L}$) in the pristine and Gr-MoS_2 heterostructure region, with Dirac points at 6.8 V and −5 V, respectively. We estimate the maximum μ to be 2340 $cm^2\,V^{-1}\,s^{-1}$ for pristine Gr and ∼3000 $cm^2\,V^{-1}\,s^{-1}$ for the Gr-MoS_2 heterostructure region. The electrical properties of the heterostructure region indicate the excellent quality of materials; even wet transfer of CVD-MoS_2 on CVD-Gr does not have a detrimental effect on its electrical transport properties [10,55]. The heterostructure devices were quite stable during the measurements, and the essential charge transport characteristics could be remeasured even several months after device fabrication, although some contact resistance and transistor properties varied with time. Development of scalable methods to encapsulate such all-CVD devices with 2D insulators (for example, with hBN) should further enhance the stability of devices.

B. Spin transport and precession across the all-CVD Gr-MoS_2 vdW heterostructure

To investigate the spin dynamics in the all-CVD Gr-MoS_2 heterostructure, NL spin-transport measurements [Fig. 2(a)] were carried out with varying magnetic fields (B) along different directions. We adopted NL measurement geometry, where the injected current and detected voltage circuits are secluded to detect pure spin-polarized current. SV measurements are performed to detect in-plane spin transport in the

Gr-MoS_2 heterostructure channel, where B_y field is applied along the magnetic easy axis of the FM contacts to switch their magnetization. The switching of the FM contacts renders a SV signal between parallel and antiparallel magnetization states of the injector and detector FM contacts. Figure 2(b) shows the NLSV signal in Device 1 of the Gr-MoS_2 heterostructure with a channel length $L = 9.6\,\mu\text{m}$.

Next, we measured the Hanle spin-precession signal by applying a perpendicular magnetic field (B_z) to the Gr-MoS_2 plane. In this measurement geometry, the magnetic field dephases the diffusing spins in the channel and renders a cosine-dependent Hanle spin-precession signal that diminishes with increasing magnetic field. Figure 2(c) shows the measured Hanle signals for parallel and antiparallel FM magnetizations along with the fitting with Eq. (1) [2,56]:

$$R_{\text{nl}} \propto \int_0^\infty \frac{1}{\sqrt{4\pi D_s t}} \exp\left(-\frac{L^2}{4D_s t}\right) \cos(\omega_L t) \exp\left(-\frac{t}{\tau_s}\right) dt. \tag{1}$$

Here, $\omega_L = \frac{g\mu_B}{\hbar} B_\perp$ is the Larmor frequency, where $B_\perp$ is a perpendicular magnetic field applied to the easy axis of the FM contacts, $g = 2$ is assumed, D_s is the spin diffusion constant, and $\lambda_s = \sqrt{D_s\,\tau_s}$ and τ_s are the transverse spin-diffusion length and lifetime in Gr, respectively. The fitting parameters provide spin-transport parameters in the xy plane. We found that the in-plane spin lifetime in the Gr-MoS_2 heterostructure channel is about $\tau_\parallel = 125 \pm 6\,\text{ps}$, and spin-diffusion length $\lambda_\parallel = 2.2 \pm 0.13\,\mu\text{m}$. Here, D_s is found in a similar range ($0.022\,\text{m}^2\,\text{s}^{-1}$) at $V_g = 40\,\text{V}$ as the charge diffusion constant ($D = 0.025\,\text{m}^2\,\text{s}^{-1}$), as expected for Gr on SiO_2 [57].

Next, we investigated the influence of the gate electric field on the Hanle spin-precession signal in the Gr-MoS_2 heterostructure (Device 2) with a channel length of 10.6 μm. The Dirac curve of the heterostructure region is presented in Fig. 2(d), where the Dirac point of Gr is $V_g \sim 7\,\text{V}$, and mobility is estimated to be $\sim 2700\,\text{cm}^2\,\text{V}^{-1}\,\text{s}^{-1}$. Figure 2(e) shows the evolution of the Hanle spin-precession signal measured with different V_g at room temperature. The amplitude (ΔR_{nl}) and extracted spin parameters from the Hanle spin-precession measurements at different V_g are shown in the panels in Fig. 2(f). It is noticeable that λ_s, D_s, and τ_s are steady at ~ 1.35 μm, $0.01\,\text{m}^2\,\text{s}^{-1}$, and 160 ps, respectively, in the higher V_g range. However, near the Dirac point, a reduction of all spin parameters is observed, which can be originated from the conductivity mismatch between FM injector and detector contacts on the Gr channel [58,59].

The spin-transport studies in exfoliated Gr-MoS_2 heterostructures showed spin field-effect functionality, where the spin signal in the channel could be controlled by an application of the gate electric field [38,39]. The reduction of the in-plane spin lifetime in the heterostructures can be attributed to proximity SOC and spin-relaxation anisotropy. The gate tunability of spin parameters can be attributed to the variable degree of spin absorption from Gr into the TMDC, governed by the gate-dependent Schottky barrier strength at the Gr-MoS_2 interface and by the strong modulation of MoS_2 conductivity because of its n-type properties. Contrary to these studies in exfoliated Gr-TMDC samples, where the gate-dependent spin transport showed the disappearance of the spin signals at the higher positive gate voltages [38,39,48], the all-CVD Gr-MoS_2 samples exhibited the spin signals to be present also at higher gate voltages. The observation of spin signals at higher V_g in the all-CVD sample indicates the absence of the tunable spin absorption effect by CVD-MoS_2 on the CVD-Gr channel. Moreover, spin absorption by CVD-MoS_2 on the CVD-Gr channel in our device might be effective in all gate voltages [60,61]. This behavior can be understood from the very low Schottky barrier estimated in our all-CVD MoS_2/Gr interfaces with $\Phi_B \sim 20\,\text{meV}$ (to be reported elsewhere) in comparison with $\sim$100 meV obtained in previous exfoliated MoS_2/Gr samples [38,39,48] in the flat band conditions [51,52].

Spin scattering in the all-CVD Gr-MoS_2 channel is evaluated by considering two main spin-relaxation mechanisms, i.e., Elliott-Yafet (EY) and D'yakonov-Perel' (DP). Here, EY includes the spin-flip events that are due to momentum scattering (τ_p), where τ_s is proportional to τ_p. On the other hand, DP accounts for the spin-scattering events due to an effective magnetic field between the momentum scattering events, where τ_s is inversely proportional to τ_p. The SOC can be correlated to these scattering mechanisms, which can be expressed as $\tau_{s,\text{DP}}^{-1} = 4(\frac{\Delta_{\text{DP}}}{\hbar})^2 \tau_p$ and $\tau_{s,\text{EY}} = (\frac{E_F}{\Delta_{\text{EY}}})^2 \tau_p$. Here, E_F is the relative Fermi energy in Gr with respect to the Dirac point, and Δ_{EY} and Δ_{DP} are energy scales due to EY and DP mechanisms, respectively. The total spin lifetime in the channel can be expressed as $\tau_s = (\tau_{s,\text{EY}}^{-1} + \tau_{s,\text{DP}}^{-1})^{-1}$, which yields [56,62,63]

$$E_F^2 \frac{\tau_p}{\tau_s} = \Delta_{\text{EY}}^2 + 4\left(\frac{\Delta_{\text{DP}} E_F \tau_p}{\hbar}\right)^2. \tag{2}$$

Figure 2(g) shows the estimated data points along with the fitting to Eq. (2), and we found $\Delta_{\text{EY}} = 488\,\mu\text{eV}$ and $\Delta_{\text{DP}} = 227\,\mu\text{eV}$. The estimated DP strength mainly incorporates SOC due to broken inversion symmetry [64], which resembles Rashba SOC that turns the spin orientation toward the Gr plane. In addition to the Rashba SOC, MoS_2 can imprint spin-valley coupling due to the Zeeman effect that turns the spin orientation toward the out-of-plane (z axis) direction, and the associated strength is discussed in a later section.

C. Spin transport and precession in pristine CVD Gr

As a reference, we measured spin transport in a pristine CVD Gr channel [Fig. 3(a)] to compare with the heterostructure. NLSV and Hanle spin-precession signals are presented in Figs. 3(b) and 3(c), respectively. The gate dependence of pristine Gr channel resistivity is shown in the top panel of Fig. 3(d), where the channel length is ~ 6 μm, the field-effect mobility is calculated to be $\sim 3000\,\text{cm}^2\,\text{V}^{-1}\,\text{s}^{-1}$, and the Dirac point voltage is $V_d = 30\,\text{V}$. The extracted spin parameters λ_s, D_s, and τ_s from the Hanle signals as a function of V_g are presented sequentially in Fig. 3(d). At higher gate voltages, away from the Dirac point, the spin parameters in the Gr remain unchanged. For instance, τ_s, D_s, and λ_s are $\sim$420 ps, $0.03\,\text{m}^2\,\text{s}^{-1}$, and 4.21 μm, respectively, at $V_g \leqslant -30\,\text{V}$. However, near the Dirac point of the Gr channel, the lowest values of all parameters are observed. The spin-transport

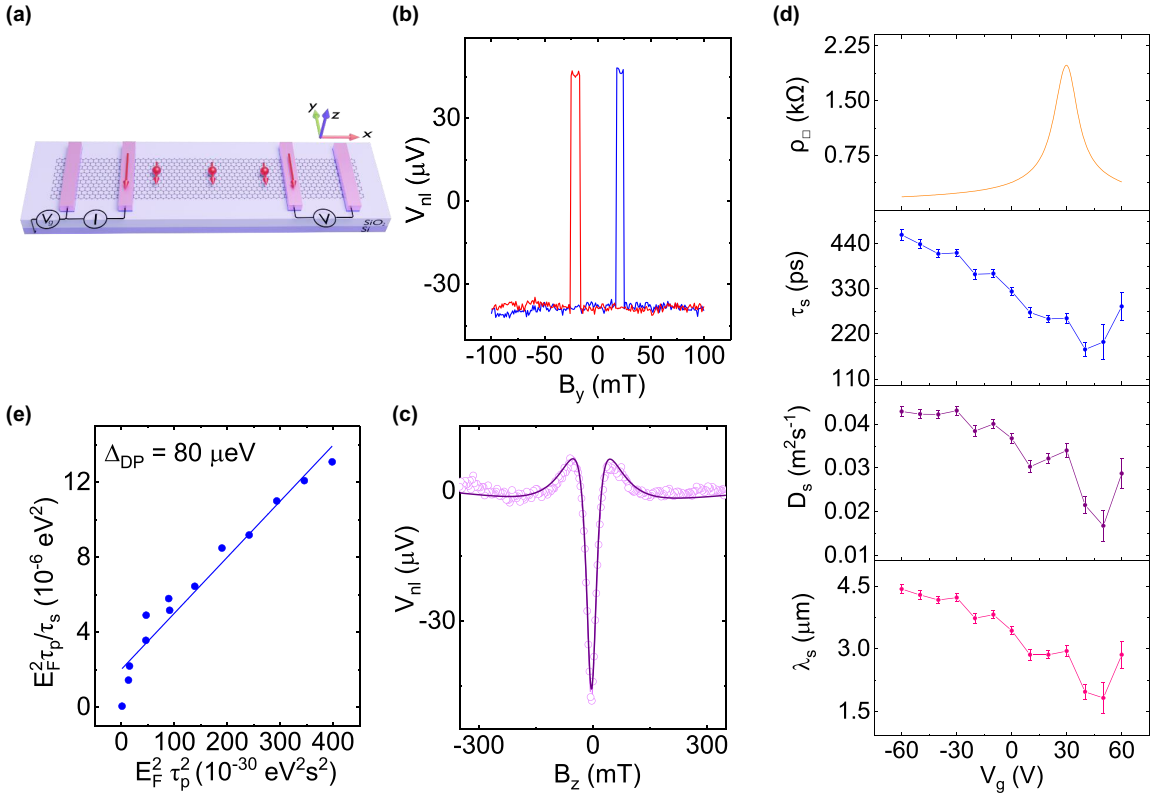

FIG. 3. Spin-transport parameters in pristine chemical vapor-deposited (CVD) graphene (Gr) at room temperature. (a) A schematic representation of the device with a pristine Gr channel and the measurement geometry with injector and detector ferromagnetic (FM) contacts. (b) Nonlocal (NL) spin-valve measurement with changing magnetic field along the y axis (magnetic easy axis). (c) NL Hanle spin-precession signal with changing magnetic field along the out-of-plane direction (z axis). (d) Gate-dependent channel resistivity of Gr along with extracted spin-diffusion length (λ_s), diffusion constant (D_s), and spin lifetime (τ_s) from the Hanle signals. (e) Estimation of spin-orbit coupling (SOC) strength in pristine Gr channel along with fitting (solid line) to Eq. (2). Measurements were performed with bias current $I = -100\,\mu$A at room temperature.

parameters start to increase again at $V_g \geqslant 60$ V due to the reduction of Gr channel resistivity, ameliorating the conductivity mismatch issue between Gr and injector and detector FM contacts [58,59]. The extracted SOC strength in pristine Gr due to EY and DP spin-relaxation mechanisms [using Eq. (2)] are $\Delta_{EY} = 1.43$ meV and $\Delta_{DP} = 80\,\mu$eV [Fig. 3(e)]. A similar Δ_{EY} strength (≈ 0.5–1.5 meV) is reported in pristine Gr on SiO_2 and hBN, which can be attributed to the nonproximity-induced SOC scattering mechanisms [62,63]. We observed significantly higher Δ_{DP} in the Gr-MoS_2 heterostructure region due to the strong proximity effect, which is $\sim 3\times$ higher than what is manifested in pristine Gr.

Proximity-induced SOC phenomena in heterostructures of Gr with high-SOC materials like TMDCs and TIs have been extensively studied both theoretically and experimentally; however, these studies were mostly limited to exfoliated flakes [35–37,63,65]. These proximity-induced SOCs in Gr have been explored experimentally by weak antilocalization, spin-relaxation anisotropy, and penetration field capacitance measurements [34,37,48]. The proximity-induced SOC strength was estimated to be a few meV [25,26] in comparison with ~ 40 μeV of the intrinsic SOC in pristine Gr [66]. For instance, spin-transport studies in Gr-MoS_2 heterostructures showed a reduction of spin lifetime with estimated SOC strength of ~ 1 meV [38,39], where the spin field-effect switch functionality is attributed to spin absorption and spin-relaxation anisotropy.

D. Spin-valley coupling and spin-lifetime anisotropy in all-CVD Gr-MoS_2 heterostructure

It is predicted that Gr in proximity to high-SOC materials can give rise to large spin-lifetime anisotropy ($\xi = \frac{\tau_\perp}{\tau_\parallel}$), mainly by means of induced Rashba SOC or spin-valley coupling [67]. The SOC associated with Rashba spin-split bands gives rise to a higher in-plane spin lifetime ($\tau_\parallel > \tau_\perp$) and anisotropy of less than unity ($\xi < 1$). On the other hand, induced spin-valley coupling in the heterostructure renders higher out-of-plane spin polarization ($\tau_\parallel < \tau_\perp$) and results in $\xi > 1$ because of dominant out-of-plane spin polarization in different valleys (K and K') of the TMDC [32,48,64]. To verify the SOC mechanisms in an all-CVD Gr-MoS_2 heterostructure, we estimated ξ by employing oblique magnetic-field-dependent evolution of Hanle spin-precession signals [68]. In this measurement scheme [Fig. 4(a)], the changing magnetic field (B) is applied at an angle (β) to the FM contact in the yz plane and lets the spins, perpendicular to the external magnetic field, to dephase. Hence, the

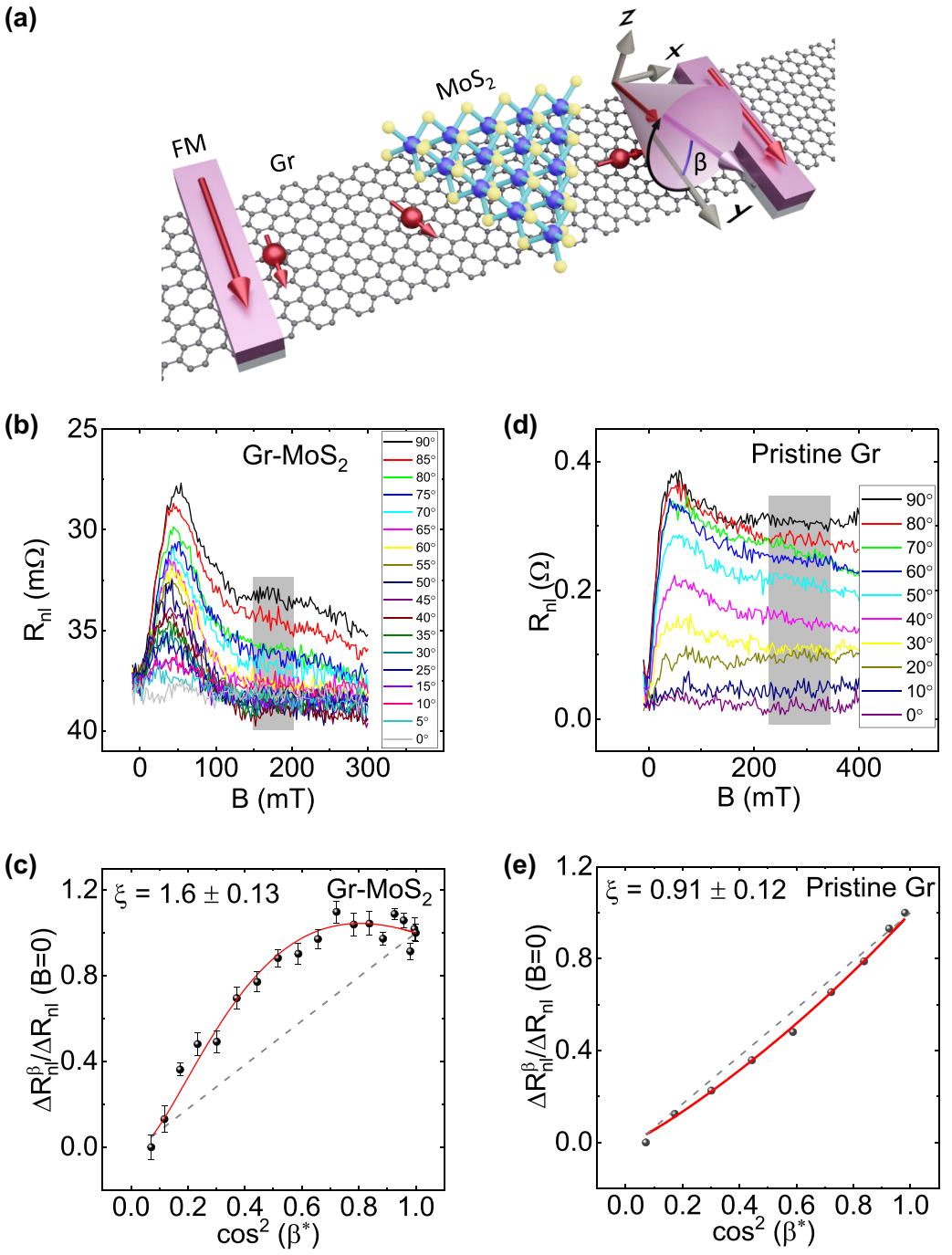

FIG. 4. Spin-lifetime anisotropy in all–chemical vapor-deposited (CVD) graphene (Gr)-MoS_2 heterostructure at room temperature. (a) Schematic illustration of the device and measurement scheme for spin-precession in Gr-MoS_2 heterostructure with an oblique magnetic field. The applied magnetic field is at an angle β along the magnetic easy axis of the ferromagnetic (FM) contacts (y axis) in the yz plane. (b) Spin-precession signals as a function of changing B field at different angles in Device 1 with $I = -350\,\mu$A at $V_g = 40$ V at room temperature. (c) Data points denote normalized nonlocal (NL) resistances ($R_{nl,\beta}/R_{nl,0}$) as a function of $\cos^2(\beta^*)$ along with the fitting (red line) to Eq. (3) to estimate anisotropy. (d) Spin-precession signals as a function of changing B field at different angles with $I = -100\,\mu$A at $V_g = 20$ V in pristine Gr. (e) Data points denote normalized NL resistances ($R_{nl,\beta}/R_{nl,0}$) as a function of $\cos^2(\beta^*)$ along with the fitting (solid line) to Eq. (3) to estimate anisotropy in pristine Gr. The dashed lines in (c) and (e) visualize the isotropic case.

manifested NL spin signal only measures the projection of the dephashed spin onto that applied field direction. Figure 4(b) shows measured Hanle spin-precession signals for different magnetic field directions.

Figure 4(c) shows the normalized value of the NL resistances ($R_{nl,\beta}/R_{nl,0}$) as a function of $\cos^2(\beta^*)$ for the respective applied field (B) direction in the dephased regime, which is highlighted by the shaded region in Fig. 4(b). Here, β^* is the

angle with a smaller correction of the out-of-plane tilting angle of the FM contacts due to the external magnetic field [68]. The average value of data points is accounted to reduce the effect of the measurement noise in the analysis. We fitted the data points with the following Eq. (3) [48,55,68] [Fig. 4(c)]:

$$\frac{R_{\rm nl}^{\beta}}{R_{\rm nl}^{0}} = \sqrt{\cos^2(\beta)+\frac{1}{\xi}\sin^2(\beta)}^{-1} \times \exp\left\{-\frac{L}{\lambda_{\parallel}}\left[\sqrt{\cos^2(\beta)+\frac{1}{\xi}\sin^2(\beta)}-1\right]\right\}\cos^2(\beta^*). \tag{3}$$

Here, L represents the heterostructure channel length, and $\lambda_{\parallel}$ is the in-plane spin-diffusion length. We found anisotropy $\xi \approx 1.6 \pm 0.13$ in the Gr-MoS_2 heterostructure channel. In the derivation of Eq. (3), the g-factor is considered isotropic and equal to the free electron value [68]. The g-factor is intrinsic to the material properties and can be anisotropic along different orientations [69,70], but the anisotropy component of the g-factor is ∼2 orders of magnitude lower than the isotropic part and can be disregarded, as also discussed in the literature [71,72].

Next, we estimated the spin-valley coupling in the Gr-MoS_2 heterostructure by using the following equation [32,67]:

$$\xi = \left(\frac{\lambda_{\rm VZ}}{\lambda_{\rm R}}\right)^2 \frac{\tau_{\rm iv}}{\tau_{\rm p}} + \frac{1}{2}. \tag{4}$$

Here, λ_{VZ} and λ_R are the valley Zeeman and Rashba SOC constants; $\tau_{\rm iv}$ and $\tau_{\rm p}$ are the intervalley and momentum-scattering lifetimes. We found $\lambda_{VZ} \sim 238$ μeV by cosidering $\tau_{\rm iv} \approx \tau_{\rm p}$ and $\lambda_R = 227$ μeV. The exact ratio of $\frac{\tau_{\rm iv}}{\tau_{\rm p}}$ is difficult to estimate; however, the relatively lower ξ must be compatible with our assumption, whereas the theoretical study reports an anisotropy of $\xi \approx 20$, considering $\tau_{\rm iv} \approx 5\tau_{\rm p}$ [67]. We also compared the estimated anisotropy in pristine Gr by measuring oblique Hanle spin signals in different magnetic field directions, as shown in Fig. 4(d). Figure 4(e) shows the normalized value of the NL resistances ($R_{{\rm nl},\beta}/R_{{\rm nl},0}$) as a function of $\cos^2(\beta^*)$ for the respective B direction in the fully dephased regime, which is highlighted by the shaded region in Fig. 4(d). The fit to Eq. (3) with the data points provides an estimation of anisotropy close to unity $\xi \approx 0.91 \pm 0.12$, shown in Fig. 4(e). It is expected that Gr on a SiO_2 substrate with a lower SOC should render isotropic spin lifetime [55,67].

According to the theoretical calculations and recent experiments in exfoliated Gr-TMDC heterostructures, the anisotropy ξ can be in the range of 1–10 [45,48,64,67]. For instance, exfoliated Gr-$MoSe_2$ and Gr-WSe_2 heterostructures show $\xi > 10$ at 75 K, whereas the Gr-WS_2 heterostructure shows $\xi \approx 10$ at room temperature [48,64]. Furthermore, the anisotropy in the exfoliated Gr-MoS_2 heterostructure is estimated to be higher than unity ($\xi > 1$) at room temperature [48]. We estimated spin-lifetime anisotropy of $\xi = 1.6$ in the all-CVD Gr-MoS_2 heterostructure using oblique Hanle measurements, which can be due to proximity-induced spin-valley locking in Gr from MoS_2. Interestingly, the anisotropy in the Gr-TMDC heterostructure significantly depends on the intervalley ($\tau_{\rm iv}$) and momentum scattering (τ_p) lifetimes, which also depend on the charge scatterers in the spin-transport channel [67]. The proximity SOC strength and anisotropy can also be influenced by the interfacial interstitials, twist-angle, and band alignment in the all-CVD Gr-TMDC heterostrcuture channels [49,73].

III. METHODS

The devices were fabricated using all-CVD-grown monolayer Gr and MoS_2. The 4-inch wafer-scale CVD Gr was obtained from Graphenea on a highly doped Si/SiO_2 substrate (with a thermally grown 285-nm-thick SiO_2 layer). First, Gr stripes were patterned by electron beam lithography and oxygen plasma etching and cleaned afterward by acetone and isopropyl alcohol (IPA). The CVD monolayer MoS_2 layers of triangular shape with a typical size of ∼50–100 μm were grown by the CVD process, as described in Refs. [74,75] on a SiO_2 (300 nm)/Si substrate. A wet-transferred technique was employed to transfer CVD MoS_2 on top of patterned CVD-Gr stripes [49]. Appropriate heterostructure regions were identified by an optical microscope for device fabrication. We used electron-beam lithography to define the contacts and e-beam evaporation for depositing the contacts. We prepared ∼1 nm of TiO_2 tunnel barrier with deposition of Ti followed by *in situ* oxidation for 30 min. We deposited Co contacts of 80-nm thickness without breaking the vacuum, followed by the liftoff process in warm acetone at 65 °C. The Co/TiO_2 contacts serve as injector and detector for spin-polarized carriers, and the highly doped Si/SiO_2 is used as a back gate. We found the FM contact resistances with three-terminal measurement geometry ∼3–8 kΩ. We used a Keithley 6221 current source to apply bias current, Keithley 2182A nanovoltmeter to detect voltage, and Keithley 2450 sourcemeter to apply back gate. The transport measurements were conducted in a vacuum cryostat at room temperature with the sample stage rotation facilities and a variable magnetic field.

IV. SUMMARY

We demonstrated spin-valley coupling and spin-relaxation anisotropy in scalable all-CVD-grown Gr-MoS_2 vdW heterostructure devices at room temperature. The CVD-grown materials and their heterostructures showed excellent charge and spin-transport properties, showing the good quality of the hybrid devices and interfaces. The spin transport and Hanle spin-precession measurements in the heterostructure channel showed increased SOC strength in the proximitized Gr, which is 3× higher than that in pristine Gr. The spin-relaxation anisotropy properties evaluated using oblique Hanle spin-precession measurements revealed an anisotropic spin dynamic of $\xi \sim 1.6$ in the proximitized Gr compared with $\xi \sim 1$ in the pristine Gr channel. The associated spin-valley coupling strength of 238 μeV is estimated in the all-CVD Gr-MoS_2 heterostructure. The observation of increased SOC strength and spin-relaxation anisotropy between the in-plane and perpendicular spin polarization in all-CVD Gr-MoS_2 heterostructures has enormous prospects for making spin-filtering devices with scalable all-2D materials. These advances will open opportunities to utilize all-CVD vdW

heterostructures for the development of next-generation scalable spintronic and quantum devices.

The data that support the findings of this study are available from the corresponding author on reasonable request.

ACKNOWLEDGMENTS

The authors acknowledge financial support from FlagEra project H2O (funded by VR), 2D TECH VINNOVA competence center (No. 2019-00068), EU Graphene Flagship (Core 3, No. 881603), Swedish Research Council VR project grants (No. 2021–04821), FLAG-ERA project 2DSOTECH (VR No. 2021–05925), Graphene center, EI Nano, and AoA Materials and AoA Energy programs at Chalmers University of Technology. This paper was also supported by the Deutsche Forschungsgemeinschaft through SPP2244 "2D Materials—Physics of van der Waals [hetero]structures" (TU149/13-1, Project No. 443361515) and through the individual research grant TU149/16-1, Project No. 464283495. We acknowledge the help of staff at the Quantum Device Physics laboratory and Nanofabrication laboratory in our Department of Microtechnology and Nanoscience at the Chalmers University of Technology.

The authors declare no competing interests.

[1] B. Behin-Aein, D. Datta, S. Salahuddin, and S. Datta, Proposal for an all-spin logic device with built-in memory, Nat. Nanotechnol. **5**, 266 (2010).

[2] I. Žutić, J. Fabian, and S. Das Sarma, Spintronics: Fundamentals and applications, Rev. Mod. Phys. **76**, 323 (2004).

[3] X. Lin, W. Yang, K. L. Wang, and W. Zhao, Two-dimensional spintronics for low-power electronics, Nat. Electron. **2**, 274 (2019).

[4] B. Dieny, I. L. Prejbeanu, K. Garello, P. Gambardella, P. Freitas, R. Lehndorff, W. Raberg, U. Ebels, S. O. Demokritov, J. Akerman *et al.*, Opportunities and challenges for spintronics in the microelectronics industry, Nat. Electron. **3**, 446 (2020).

[5] Y. Lei, T. Zhang, Y.-C. Lin, T. Granzier-Nakajima, G. Bepete, D. A. Kowalczyk, Z. Lin, D. Zhou, T. F. Schranghamer, A. Dodda *et al.*, Graphene and beyond: Recent advances in two-dimensional materials synthesis, properties, and devices, ACS Nanosci. Au. **2**, 450 (2022).

[6] S. K. Chakraborty, B. Kundu, B. Nayak, S. P. Dash, and P. K. Sahoo, Challenges and opportunities in 2D heterostructures for electronic and optoelectronic devices, iScience. **25**, 103942 (2022).

[7] B. Zhao, R. Ngaloy, S. Ghosh, S. Ershadrad, R. Gupta, K. Ali, A. M. Hoque, B. Karpiak, D. Khokhriakov, C. Polley *et al.*, A room-temperature spin-valve with van der Waals ferromagnet Fe_5GeTe_2/graphene heterostructure, Adv. Mater. 2209113 (2023).

[8] A. K. Geim and K. S. Novoselov, The rise of graphene, Nat. Mater. **6**, 183 (2007).

[9] D. Khokhriakov, S. Sayed, A. M. Hoque, B. Karpiak, B. Zhao, S. Datta, and S. P. Dash, Multifunctional Spin Logic Operations in Graphene Spin Circuits, Phys. Rev. Appl. **18**, 064063 (2022).

[10] D. Khokhriakov, B. Karpiak, A. M. Hoque, and S. P. Dash, Two-dimensional spintronic circuit architectures on large scale graphene, Carbon N. Y. **161**, 892 (2020).

[11] M. V. Kamalakar, C. Groenveld, A. Dankert, and S. P. Dash, Long distance spin communication in chemical vapour deposited graphene, Nat. Commun. **6**, 6766 (2015).

[12] M. Gmitra, S. Konschuh, C. Ertler, C. Ambrosch-Draxl, and J. Fabian, Band-structure topologies of graphene: Spin-orbit coupling effects from first principles, Phys. Rev. B. **80**, 235431 (2009).

[13] B. Karpiak, A. Dankert, A. W. Cummings, S. R. Power, S. Roche, and S. P. Dash, 1D ferromagnetic edge contacts to 2D graphene/h-BN heterostructures, 2D Mater. **5**, 014001 (2017).

[14] J. F. Sierra, J. Fabian, R. K. Kawakami, S. Roche, and S. O. Valenzuela, Van der Waals heterostructures for spintronics and opto-spintronics, Nat. Nanotechnol. **16**, 856 (2021).

[15] J. Balakrishnan, G. K. W. Koon, A. Avsar, Y. Ho, J. H. Lee, M. Jaiswal, S.-J. Baeck, J.-H. Ahn, A. Ferreira, M. A. Cazalilla *et al.*, Giant spin Hall effect in graphene grown by chemical vapour deposition, Nat. Commun. **5**, 4748 (2014).

[16] J. Balakrishnan, G. K. W. Koon, M. Jaiswal, A. H. Castro Neto, and B. Özyilmaz, Colossal enhancement of spin-orbit coupling in weakly hydrogenated graphene, Nat. Phys. **9**, 284 (2013).

[17] K. Pi, W. Han, K. M. McCreary, A. G. Swartz, Y. Li, and R. K. Kawakami, Manipulation of Spin Transport in Graphene by Surface Chemical Doping, Phys. Rev. Lett. **104**, 187201 (2010).

[18] B. Zhao, A. M. Hoque, D. Khokhriakov, B. Karpiak, and S. P. Dash, Charge-spin conversion signal in WTe_2 van der Waals hybrid devices with a geometrical design, Appl. Phys. Lett. **117**, 242401 (2020).

[19] A. M. Hoque, D. Khokhriakov, B. Karpiak, and S. P. Dash, Charge-spin conversion in layered semimetal $TaTe_2$ and spin injection in van der Waals heterostructures, Phys. Rev. Res. **2**, 033204 (2020).

[20] A. M. Hoque, B. Zhao, D. Khokhriakov, P. Muduli, and S. P. Dash, Charge to spin conversion in van der Waals metal $NbSe_2$, Appl. Phys. Lett. **121**, 242404 (2022).

[21] B. Zhao, B. Karpiak, D. Khokhriakov, A. Johansson, A. M. Hoque, X. Xu, Y. Jiang, I. Mertig, and S. P. Dash, Unconventional charge-spin conversion in Weyl-semimetal WTe_2, Adv. Mater. **32**, 2000818 (2020).

[22] Z. Kovács-Krausz, A. M. Hoque, P. Makk, B. Szentpéteri, M. Kocsis, B. Fülöp, M. V. Yakushev, T. V. Kuznetsova, O. E. Tereshchenko, K. A. Kokh *et al.*, Electrically controlled spin injection from giant Rashba spin-orbit conductor BiTeBr, Nano Lett. **20**, 4782 (2020).

[23] A. Avsar, H. Ochoa, F. Guinea, B. Özyilmaz, B. J. van Wees, and I. J. Vera-Marun, Colloquium: Spintronics in graphene and other two-dimensional materials, Rev. Mod. Phys. **92**, 021003 (2020).

[24] E. C. Ahn, 2D materials for spintronic devices, npj 2D Mater. Appl. **4**, 17 (2020).

[25] M. Gmitra and J. Fabian, Graphene on transition-metal dichalcogenides: A platform for proximity spin-orbit physics and optospintronics, Phys. Rev. B. **92**, 155403 (2015).

[26] M. Gmitra, D. Kochan, P. Högl, and J. Fabian, Trivial and inverted Dirac bands and the emergence of quantum spin Hall

states in graphene on transition-metal dichalcogenides, Phys. Rev. B. **93**, 155104 (2016).

[27] K. Song, D. Soriano, A. W. Cummings, R. Robles, P. Ordejón, and S. Roche, Spin proximity effects in graphene/topological insulator heterostructures, Nano Lett. **18**, 2033 (2018).

[28] D. Khokhriakov, A. M. Hoque, B. Karpiak, and S. P. Dash, Gate-tunable spin-galvanic effect in graphene-topological insulator van der Waals heterostructures at room temperature, Nat. Commun. **11**, 3657 (2020).

[29] A. M. Hoque, D. Khokhriakov, K. Zollner, B. Zhao, B. Karpiak, J. Fabian, and S. P. Dash, All-electrical creation and control of spin-galvanic signal in graphene and molybdenum ditelluride heterostructures at room temperature, Commun. Phys. **4**, 124 (2021).

[30] Y. Cao, V. Fatemi, A. Demir, S. Fang, S. L. Tomarken, J. Y. Luo, J. D. Sanchez-Yamagishi, K. Watanabe, T. Taniguchi, E. Kaxiras *et al.*, Correlated insulator behaviour at half-filling in magic-angle graphene superlattices, Nature (London) **556**, 80 (2018).

[31] Y. Cao, V. Fatemi, S. Fang, K. Watanabe, T. Taniguchi, E. Kaxiras, and P. Jarillo-Herrero, Unconventional superconductivity in magic-angle graphene superlattices, Nature (London) **556**, 43 (2018).

[32] J. H. Garcia, M. Vila, A. W. Cummings, and S. Roche, Spin transport in graphene/transition metal dichalcogenide heterostructures, Chem. Soc. Rev. **47**, 3359 (2018).

[33] B. Szentpéteri, P. Rickhaus, F. K. de Vries, A. Márffy, B. Fülöp, E. Tóvári, K. Watanabe, T. Taniguchi, A. Kormányos, S. Csonka *et al.*, Tailoring the band structure of twisted double bilayer graphene with pressure, Nano Lett. **21**, 8777 (2021).

[34] J. O. Island, X. Cui, C. Lewandowski, J. Y. Khoo, E. M. Spanton, H. Zhou, D. Rhodes, J. C. Hone, T. Taniguchi, K. Watanabe *et al.*, Spin–orbit-driven band inversion in bilayer graphene by the van der Waals proximity effect., Nature (London) **571**, 85 (2019).

[35] B. Fülöp, A. Márffy, S. Zihlmann, M. Gmitra, E. Tóvári, B. Szentpéteri, M. Kedves, K. Watanabe, T. Taniguchi, J. Fabian *et al.*, Boosting proximity spin-orbit coupling in graphene/WSe_2 heterostructures via hydrostatic pressure, npj 2D Mater. Appl. **5**, 82 (2021).

[36] Z. Wang, D. Ki, H. Chen, H. Berger, A. H. MacDonald, and A. F. Morpurgo, Strong interface-induced spin-orbit interaction in graphene on WS_2, Nat. Commun. **6**, 8339 (2015).

[37] Z. Wang, D. K. Ki, J. Y. Khoo, D. Mauro, H. Berger, L. S. Levitov, and A. F. Morpurgo, Origin and Magnitude of 'Designer' Spin-Orbit Interaction in Graphene on Semiconducting Transition Metal Dichalcogenides, Phys. Rev. X. **6**, 041020 (2016).

[38] W. Yan, O. Txoperena, R. Llopis, H. Dery, L. E. Hueso, and F. Casanova, A two-dimensional spin field-effect switch, Nat. Commun. **7**, 13372 (2016).

[39] A. Dankert and S. P. Dash, Electrical gate control of spin current in van der Waals heterostructures at room temperature, Nat. Commun. **8**, 16093 (2017).

[40] Y. K. Luo, J. Xu, T. Zhu, G. Wu, E. J. McCormick, W. Zhan, M. R. Neupane, and R. K. Kawakami, Opto-valleytronic spin injection in monolayer MoS_2/few-layer graphene hybrid spin valves, Nano Lett. **17**, 3877 (2017).

[41] C. K. Safeer, J. Ingla-Aynés, F. Herling, J. H. Garcia, M. Vila, N. Ontoso, M. R. Calvo, S. Roche, L. E. Hueso, and F. Casanova, Room-temperature spin Hall effect in graphene/MoS_2 van der Waals heterostructures, Nano Lett. **19**, 1074 (2019).

[42] L. A. Benítez, W. Savero Torres, J. F. Sierra, M. Timmermans, J. H. Garcia, S. Roche, M. V. Costache, and S. O. Valenzuela, Tunable room-temperature spin galvanic and spin Hall effects in van der Waals heterostructures, Nat. Mater. **19**, 170 (2020).

[43] T. S. Ghiasi, A. A. Kaverzin, P. J. Blah, and B. J. van Wees, Charge-to-spin conversion by the Rashba-Edelstein effect in two-dimensional van der Waals heterostructures up to room temperature, Nano Lett. **19**, 5959 (2019).

[44] A. Avsar, D. Unuchek, J. Liu, O. L. Sanchez, K. Watanabe, T. Taniguchi, B. Özyilmaz, and A. Kis, Optospintronics in graphene via proximity coupling, ACS Nano. **11**, 11678 (2017).

[45] L. A. Benítez, J. F. Sierra, W. Savero Torres, M. Timmermans, M. V. Costache, and S. O. Valenzuela, Investigating the spin-orbit interaction in van der Waals heterostructures by means of the spin relaxation anisotropy, APL Mater. **7**, 120701 (2019).

[46] J. R. Schaibley, H. Yu, G. Clark, P. Rivera, J. S. Ross, K. L. Seyler, W. Yao, and X. Xu, Valleytronics in 2D materials, Nat. Rev. Mater. **1**, 16055 (2016).

[47] K. F. Mak, K. He, J. Shan, and T. F. Heinz, Control of valley polarization in monolayer MoS_2 by optical helicity, Nat. Nanotechnol. **7**, 494 (2012).

[48] L. A. Benítez, J. F. Sierra, W. Savero Torres, A. Arrighi, F. Bonell, M. V. Costache, and S. O. Valenzuela, Strongly anisotropic spin relaxation in graphene–transition metal dichalcogenide heterostructures at room temperature, Nat. Phys. **14**, 303 (2018).

[49] R. Mupparapu, T. Bucher, and I. Staude, Integration of two-dimensional transition metal dichalcogenides with Mie-resonant dielectric nanostructures, Adv. Phys. X. **5**, 1734083 (2020).

[50] B. Radisavljevic, A. Radenovic, J. Brivio, V. Giacometti, and A. Kis, Single-layer MoS_2 transistors, Nat. Nanotechnol. **6**, 147 (2011).

[51] A. Allain, J. Kang, K. Banerjee, and A. Kis, Electrical contacts to two-dimensional semiconductors, Nat. Mater. **14**, 1195 (2015).

[52] T. Kim, S. Fan, S. Lee, M.-K. Joo, and Y. H. Lee, High-mobility junction field-effect transistor via graphene/MoS_2 heterointerface, Sci. Rep. **10**, 13101 (2020).

[53] S. S. Chee, D. Seo, H. Kim, H. Jang, S. Lee, S. P. Moon, K. H. Lee, S. W. Kim, H. Choi, and M. H. Ham, Lowering the Schottky barrier height by graphene/Ag electrodes for high-mobility MoS_2 field-effect transistors, Adv. Mater. **31**, 1804422 (2019).

[54] X. Cui, G. H. Lee, Y. D. Kim, G. Arefe, P. Y. Huang, C. H. Lee, D. A. Chenet, X. Zhang, L. Wang, F. Ye *et al.*, Multi-terminal transport measurements of MoS_2 using a van der Waals heterostructure device platform, Nat. Nanotechnol. **10**, 534 (2015).

[55] D. Khokhriakov, B. Karpiak, A. M. Hoque, B. Zhao, S. Parui, and S. P. Dash, Robust spin interconnect with isotropic spin dynamics in chemical vapor deposited graphene layers and boundaries, ACS Nano. **14**, 15864 (2020).

[56] W. Han, R. K. Kawakami, M. Gmitra, and J. Fabian, Graphene spintronics, Nat. Nanotechnol. **9**, 794 (2014).

[57] T. Maassen, F. K. Dejene, M. H. D. Guimarães, C. Józsa, and B. J. Van Wees, Comparison between charge and spin transport in few-layer graphene, Phys. Rev. B **83**, 115410 (2011).

[58] E. I. Rashba, Theory of electrical spin injection: Tunnel contacts as a solution of the conductivity mismatch problem, Phys. Rev. B. **62**, R16267 (2000).

[59] A. Fert and H. Jaffrès, Conditions for efficient spin injection from a ferromagnetic metal into a semiconductor, Phys. Rev. B **64**, 184420 (2001).

[60] F. Herling, C. K. Safeer, J. Ingla-Aynés, N. Ontoso, L. E. Hueso, and F. Casanova, Gate tunability of highly efficient spin-to-charge conversion by spin Hall effect in graphene proximitized with WSe_2, APL Mater. **8**, 071103 (2020).

[61] S. Omar and B. J. Van Wees, Spin transport in high-mobility graphene on WS_2 substrate with electric-field tunable proximity spin-orbit interaction, Phys. Rev. B. **97**, 045414 (2018).

[62] M. Gurram, S. Omar, and B. J. van Wees, Electrical spin injection, transport, and detection in graphene-hexagonal boron nitride van der Waals heterostructures: Progress and perspectives., 2D Mater. **5**, 032004 (2018).

[63] D. Khokhriakov, A. W. Cummings, K. Song, M. Vila, B. Karpiak, A. Dankert, S. Roche, and S. P. Dash, Tailoring emergent spin phenomena in Dirac material heterostructures, Sci. Adv. **4**, eaat9349 (2018).

[64] T. S. Ghiasi, J. Ingla-Aynés, A. A. Kaverzin, and B. J. van Wees, Large proximity-induced spin lifetime anisotropy in transition-metal dichalcogenide/graphene heterostructures, Nano Lett. **17**, 7528 (2017).

[65] B. Yang, M.-F. Tu, J. Kim, Y. Wu, H. Wang, J. Alicea, R. Wu, M. Bockrath, and J. Shi, Tunable spin-orbit coupling and symmetry-protected edge states in graphene/WS_2, 2D Mater **3**, 031012 (2016).

[66] J. Sichau, M. Prada, T. Anlauf, T. J. Lyon, B. Bosnjak, L. Tiemann, and R. H. Blick, Resonance Microwave Measurements of an Intrinsic Spin-Orbit Coupling Gap in Graphene: A Possible Indication of a Topological State, Phys. Rev. Lett. **122**, 046403 (2019).

[67] A. W. Cummings, J. H. Garcia, J. Fabian, and S. Roche, Giant Spin Lifetime Anisotropy in Graphene Induced by Proximity Effects, Phys. Rev. Lett. **119**, 206601 (2017).

[68] B. Raes, J. E. Scheerder, M. V. Costache, F. Bonell, J. F. Sierra, J. Cuppens, J. Van de Vondel, and S. O. Valenzuela, Determination of the spin-lifetime anisotropy in graphene using oblique spin precession, Nat. Commun. **7**, 11444 (2016).

[69] M. Prada, L. Tiemann, J. Sichau, and R. H. Blick, Dirac imprints on the *g*-factor anisotropy in graphene, Phys. Rev. B. **104**, 075401 (2021).

[70] C. H. Sharma, P. Zhao, L. Tiemann, M. Prada, A. D. Pandey, A. Stierle, and R. H. Blick, Electron spin resonance in a proximity-coupled MoS_2/graphene van der Waals heterostructure, AIP Adv. **12**, 035111 (2022).

[71] R. Winkler, S. J. Papadakis, E. P. De Poortere, and M. Shayegan, Highly Anisotropic G-Factor of Two-Dimensional Hole Systems, Phys. Rev. Lett. **85**, 4574 (2000).

[72] B. Raes, A. W. Cummings, F. Bonell, M. V. Costache, J. F. Sierra, S. Roche, and S. O. Valenzuela, Spin precession in anisotropic media, Phys. Rev. B **95**, 085403 (2017).

[73] A. David, P. Rakyta, A. Kormányos, and G. Burkard, Induced spin-orbit coupling in twisted graphene-transition metal dichalcogenide heterobilayers: Twistronics meets spintronics, Phys. Rev. B **100**, 085412 (2019).

[74] A. M. van der Zande, P. Y. Huang, D. A. Chenet, T. C. Berkelbach, Y. You, G.-H. Lee, T. F. Heinz, D. R. Reichman, D. A. Muller, and J. C. Hone, Grains and grain boundaries in highly crystalline monolayer molybdenum disulphide, Nat. Mater. **12**, 554 (2013).

[75] A. George, C. Neumann, D. Kaiser, R. Mupparapu, T. Lehnert, U. Hübner, Z. Tang, A. Winter, U. Kaiser, I. Staude *et al.*, Controlled growth of transition metal dichalcogenide monolayers using Knudsen-type effusion cells for the precursors, JPhys Mater. **2**, 016001 (2019).